# The design and application of an in-laboratory diffraction-enhanced x-ray imaging instrument

Ivan Nesch,[1] Daniel P. Fogarty,[1,a)] Tochko Tzvetkov,[1] Benjamin Reinhart,[1] A. Charles Walus,[1] Gocha Khelashvili,[1,2] Carol Muehleman,[3] and Dean Chapman[4]
[1]*Nesch, LLC 9800 Connecticut Drive, Crown Point, Indiana 46307, USA*
[2]*Department of Radiation Oncology, Rush University Medical Center, 500 S. Paulina St., Chicago, Illinois 60612, USA*
[3]*Department of Biochemistry, Rush Medical College, 1735 W. Harrison St., Chicago, Illinois 60612, USA*
[4]*Department of Anatomy and Cell Biology, College of Medicine, B331 Life Sciences Building, 107 Wiggins Road, Saskatoon, Saskatchewan S7N5E5, Canada*

(Received 26 May 2009; accepted 9 August 2009; published online 14 September 2009)

We describe the design and application of a new in-laboratory diffraction-enhanced x-ray imaging (DEXI) instrument that uses a nonsynchrotron, conventional x-ray source to image the internal structure of an object. In the work presented here, a human cadaveric thumb is used as a test-sample to demonstrate the imaging capability of our instrument. A 22 keV monochromatic x-ray beam is prepared using a mismatched, two-crystal monochromator; a silicon analyzer crystal is placed in a parallel crystal geometry with the monochromator allowing both diffraction-enhanced imaging and multiple-imaging radiography to be performed. The DEXI instrument was found to have an experimentally determined spatial resolution of $160 \pm 7$ $\mu$m in the horizontal direction and $153 \pm 7$ $\mu$m in the vertical direction. As applied to biomedical imaging, the DEXI instrument can detect soft tissues, such as tendons and other connective tissues, that are normally difficult or impossible to image via conventional x-ray techniques. © *2009 American Institute of Physics.*
[doi:10.1063/1.3213621]

## I. INTRODUCTION

Investigation of the internal structure of materials using x-ray imaging has proven to be a valuable technique in many different areas of science. Recently, a variety of new x-ray imaging techniques have been developed at synchrotron radiation facilities.[1–15] Rather than primarily focusing on the absorption properties of a sample to investigate an object's internal structure, such as in a conventional radiograph, these new analyzer-based techniques utilize many of the interactions that x rays undergo with an object to allow visualization of the sample's internal structure. These relatively nondestructive imaging techniques are being investigated for use in areas such as cartilage and bone imaging,[16–28] small-animal imaging,[29–32] mammography,[33–38] and other applications.[39]

In conventional radiography, a large portion of the x-ray beam that reaches the detector after passing through the sample is a scattering component. X-ray scatter reduces the image contrast and sharpness thus resulting in a less-sensitive measurement. Analyzer-based techniques, however, are almost completely free of x-ray scatter as a result of the placement of an analyzer crystal between the sample and the x-ray detector. The analyzer crystal's narrow acceptance angle reduces the scattering component enhancing the contrast of the resultant image.

One of the first analyzer-based techniques that utilized the refractive index gradient of an object was diffraction-enhanced imaging (DEI).[1] The DEI system is typically comprised of a monochromator, object of interest, analyzer crystal, and a x-ray detector. Single-crystal materials, such as silicon, are normally chosen for both the monochromator and the analyzer crystal. The crystals are placed in a parallel crystal geometry resulting in the production of a highly parallel, monochromatic x-ray beam.

Raw images, from which a set of DEI images is then computed, are collected with the analyzer crystal placed at three positions along the nearly triangular curve (the so-called "rocking curve") of reflected intensity as a function of angle; specifically, the analyzer crystal is positioned at the left side and right side of the rocking curve and at the peak intensity.[1–3] Image collection at these points is achieved by changing the angle of the analyzer crystal to three predetermined positions along the rocking curve. The analyzer crystal's rocking-curve shape introduces sensitivity to refraction and scatter occurring within the object. Density, thickness, and/or material variations within an object will alter the direction of the x rays as they traverse the material, producing small angular variations of the transmitted x-ray beam. The steep sides of the reflectivity curve will convert these angle variations into intensity variations, thus making absorption, refraction and scattering effects visible in an image.

Recently, modifications to this technique have been explored in which the number of points collected along the rocking curve is increased—commonly referred to as multiple-image radiography (MIR).[6–8] By acquiring multiple images with the analyzer set to diffract at different points

a)Author to whom correspondence should be addressed. Electronic mail: fogarty.d@neschllc.com.

 

along the rocking curve, it is possible to separate the effects of absorption, refraction, and scattering. The ability to separately resolve these effects can deliver dramatic increases in image content and contrast over conventional radiography. The refraction images, in particular, provide edge enhancement at borders between materials of different refractive indices.

Synchrotron radiation sources have been a key component for the development of analyzer-based methodologies; however, the dependence upon these sources limits the applicability of these phase-related techniques—particularly for a clinical setting. Until now, the use of a conventional x-ray tube as the x-ray source for DEI and MIR imaging has been hindered as a result of the limited x-ray intensity and the corresponding increase in sample exposure time needed to produce a reliable contrast image. Because of the narrow acceptance angle of the analyzer crystal, DEI and MIR methods require precise positioning of the diffraction crystals (on the order of microradians). Inherent and induced thermal and mechanical instabilities that occur within the system cause small angular shifts over time. Therefore, as the exposure time of the sample increases the potential effects of instability of the diffracting crystals could increase as well. In order to overcome these instabilities a more robust crystal alignment design (or a feedback system) must be incorporated to overcome the natural fluctuations that occur within the system over time.

In the work presented here we describe the design of a new in-laboratory diffraction-enhanced x-ray imaging (DEXI) instrument that utilizes a conventional x-ray tube as its source of x rays. This first-generation platform, utilizing a low-power (2.2 kW) silver anode, has proven to be capable of imaging samples from multiple types of scientific disciplines. Through careful vibration isolation and the use of high-precision crystal-positioning stages we are able to image samples using both DEI and MIR methodologies. As a result, analyzer-based imaging experiments that were solely performed at synchrotron facilities can now be conducted in a laboratory, and potentially, in a clinical setting.

In Sec. II we describe details of the design and construction of the DEXI system—specifically the conventional x-ray tube, monochromator, sample compartment, analyzer crystal, x-ray detector, and the vibration isolation platforms. In Sec. III we detail the results of testing and characterization of the apparatus. Preliminary results are discussed, describing the system's resolution and radiation dose incident on a sample. A series of DEX images are presented of a human cadaveric thumb.

## II. INSTRUMENT DESIGN

The primary goal in the design of the experimental apparatus described here was to perform analyzer-based experiments without the use of a synchrotron radiation source. By using a conventional x-ray tube, experiments such as DEI and MIR can be conducted in a laboratory and/or clinical setting. This ability to carry out such experiments has not previously been realized for a nonsynchrotron, analyzer-based x-ray system.

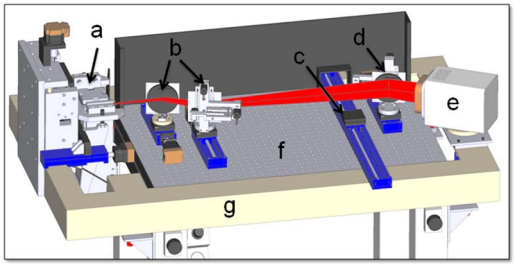


FIG. 1. (Color online) A perspective schematic of the DEXI instrument: (a) 2.2 kW Ag x-ray tube and multiaxis positioning cradle; (b) mismatched, two-crystal monochromator; (c) sample compartment; (d) analyzer crystal; (e) high-resolution, digital x-ray detector; (f) inner-vibration-isolation platform; and (g) outer-vibration-isolation platform.

Achieving this goal requires the following:

(1) a compact laboratory based x-radiation source;
(2) stable, high-precision positioning stages for accurate alignment of diffraction optics;
(3) vibration isolation of diffraction optics, sample chamber, and high-resolution x-ray detector.

With additional desired features:

(4) machine control software for both diffraction optics positioning and raw data collection;
(5) image processing software; and
(6) a safety interlock system that prevents harmful radiation exposure before, during and after DEXI operation.

All of these factors are taken into consideration and incorporated in the design of the instrument to achieve these goals.

### A. Nonsynchrotron x-ray source

A perspective diagram of the instrument is presented in Fig. 1. A mismatched, two-crystal monochromator is placed in front of the conventional x-ray source and the resulting monochromatic beam is passed through the sample.[3] An analyzer crystal is placed immediately after the sample compartment followed by a high-resolution, digital detector. The entire system is arranged on top of a self-leveling pneumatic optical table; the overall dimensions of the DEXI system is 1.2 m($h$) $\times$ 1.4 m($l$) $\times$ 0.8 m($w$).

The DEXI instrument utilizes a 2.2 kW silver anode (Panalytical, Westborough MA, USA). It is powered using a 60 kV/125 mA high-voltage power supply (Universal Voltronics, Brookfield CT, USA) and is typically operated at a voltage of 55 kV and a current of 35 mA. The x-ray tube and its' accompanied housing is held in an automated multiaxis positioning cradle that is attached securely to the outer-vibration-isolation table [Fig. 1(a)]; the x-ray source is held at an angle of ~6° resulting in a focal spot of 0.1 $\times$ 12.0 mm$^2$.

### B. Mismatched, two-crystal monochromator

A two-crystal monochromator is placed directly in front of the conventional x-ray source to select the desired 22 keV, Ag $K\alpha 1$ characteristic line [Fig. 1(b)].[3] The monochromator is made up of two mismatched crystals—a 100 mm diameter germanium (1,1,1) orientation crystal followed by a 100 mm diameter silicon (1,1,1) oriented crystal. In both crystals the

[3,3,3] reflection is used. A horizontal diffraction plane is chosen for convenience. Each crystal is held in place using a high-resolution positioning (HRP) stage attached to a 200 mm linear stage (General Controls Electronics, Elk Grove Village IL, USA).[40] The HRP stages provide automated positioning of both crystals along the tilt ($\chi$) and the rotation ($\theta$) axes with ~0.06 $\mu$rad resolution. Lead barriers designed specific to the footprint and position of the diffraction crystals are placed to minimize unwanted scattered radiation originating upstream from the monochromator. The resultant x-ray beam field of view at the sample compartment is approximately 12 mm wide by 60 mm tall.

### C. Sample compartment

The sample compartment is based on an 800 mm linear stage that enables the specimen to be moved in and out of the path of x rays exiting the monochromator [Fig. 1(c)]. The automated linear stage is attached to the outer-vibration-isolation table and is decoupled from the diffraction optics—reducing vibrations resulting from sample positioning. Separate attachments, such as rotational stages and vertical positioning stages, have been designed to provide additional positioning alternatives for imaging of a complex object. Samples are introduced to the instrument through the designated loading region of the instrument, which measures $200 \times 200$ mm$^2$. Present maximum object dimensions are 250 mm in length and/or 150 mm in height. The maximum allowable thickness of a sample depends on the linear attenuation coefficient of the specimen.

### D. Analyzer crystal and high-resolution, digital detector

A 100 mm diameter silicon (1,1,1) oriented crystal—the analyzer crystal—is placed immediately after the sample compartment, followed by a high-resolution digital detector [Fig. 1(d)]. The analyzer crystal is held in place using an HRP stage; this stage is identical to those used in the fore mentioned monochromator providing a method of precise automated positioning of the diffraction optics. The HRP stage is attached directly to a 200 mm linear stage which allows the crystal to be centered with respect to the monochromatic x-ray beam.

A digital x-ray detector (Apex II by Bruker AXS, Madison WI, USA) is used to collect the raw data. The x-ray detector is placed directly after the analyzer crystal with its face at normal incidence to the diffracted beam [Fig. 1(e)]. The detector has a software selectable pixel size of 240, 120, 60, 30, and 15 $\mu$m with a phosphorous screen point spread function of 75 $\mu$m [(full width half max (FWHM)]. Currently, the detector is operated at a pixel resolution of $1024 \times 1024$ mode which corresponds to a 60 $\mu$m pixel size.

### E. Vibration-isolation platforms

Vibration isolation is especially important in the design of the instrument as essential elements of the system (i.e., the high-voltage power supply and the water chiller), as well as ambient sources, may introduce vibrational noise. A variety of methods were employed to isolate the diffraction optics from these vibrations.

Primary vibration isolation is accomplished by placing the diffraction optics—the monochromator and the analyzer crystal—on a self-leveling, pneumatic vibration isolation table [Fig. 1(f)]. A VIBRAPLANE workstation (9100 Series) manufactured by Kinetic Systems is used as the primary platform for the DEXI system. A second, independent, pneumatic vibration-isolation platform is attached to the steel support frame of the workstation (Fig. 1(g)). Attached to the outer platform are the conventional x-ray source, sample compartment, high-resolution digital detector, and lead safety shielding. It has been found that operating the instrument without the vibration isolation platforms activated reduces the intensity of the diffracted x-ray beam by ~30% or more depending upon laboratory conditions. This independent design provides a method for decoupling those elements of the instrument that are significant sources of vibrational noise from the diffraction optics.

### F. DEX imaging software

The image collection is controlled by an in-house software program that is specifically designed for this system (written in LABVIEW; National Instruments, Austin TX, USA). The software allows the user to control all aspects of the instrument enabling complete automated control of all components. An image processing module—allowing processing of both DEI and MIR images—has been developed in-house using previously published processing methodologies for analyzer-based imaging.[2,6]

## III. EXPERIMENTAL METHOD AND EXAMPLE DATA

### A. General DEXI operating protocol

The general DEXI operating protocol requires that the user selects three parameters: (1) number of angular positions the analyzer crystal will be placed at along the rocking curve; (2) number of sample positions (translational and/or rotational) for the object of interest to be placed at during the experiment; and (3) exposure time. After image acquisition is complete the user can choose from a number of image processing methods.

Depending upon the mode of operation (DEI, MIR, etc.), the number of analyzer-crystal angular positions could range from a single position to multiple positions along the rocking-curve profile.[1–3,6] After the angular positions and the sample's translational (and/or rotational) positions are determined, the user will then choose the desired exposure time per angular position and then start the experiment. A preview option allows the user to determine an appropriate exposure time.

The control software positions the sample and adjusts the analyzer crystal's angular position according to the user's input parameters. Once the experiment has ended, the raw data is processed using the image processing module which computes the several types of DEX images—apparent absorption and refraction (DEI), extinction, refraction, ultrasmall

angle scattering (MIR), and/or scatter rejection. [No computations are required for scatter-rejection images.]

### B. DEX imaging resolution

The experimental resolution of the instrument was determined by imaging a 0.01-mm-thick, tungsten-carbide blade. A scatter-rejection image (analyzer crystal is positioned at the maximum peak intensity of the rocking curve) was taken of the tungsten-carbide blade. The resulting image was used to calculate the line spread function (LSF) of the machine. This was accomplished by first measuring the edge spread function (ESF), line-by-line, across the entire scatter-rejection image. The measured ESFs were then averaged and the digital derivative of the averaged ESF was calculated to determine the LSF of the instrument. It was found that the FWHM of the instrument's LSF is $160 \pm 7$ $\mu$m in the horizontal direction and $153 \pm 7$ $\mu$m in the vertical direction.

The calculated LSF in the vertical and horizontal directions demonstrates that the LSF is symmetrical within the precision of our instrument. The calculated spatial resolution of the instrument is expected to hold for both single-image and multiple-image modalities. Experimentally it has been found that samples that have a large index of refraction (on the order of 10 $\mu$rad) produce a shift in the image position of less than 1 $\mu$m. These resultant shifts in image position are much smaller than the spatial resolution of the x-ray detector; therefore, the calculated spatial resolution of $160 \pm 7$ $\mu$m in the horizontal direction and $153 \pm 7$ $\mu$m in the vertical direction represents the spatial resolution for both single-image and multiple-imaging modes.

### C. DEX imaging photon flux

Monte Carlo (MC) simulations have been performed to estimate the amount of radiation exposure a $10 \times 10 \times 10$ cm$^3$ tissuelike material is subject to when imaged with our DEXI instrument (22 keV). Our calculations show that our instrument delivers significantly less radiation (0.89 mGy) compared to a typical conventional mammography scan of the same tissue (3–4 mGy).[41]

For these calculations, incident fluence rates were experimentally measured and used in conjunction with MC simulations. MC code EGSnrc/DOSXYZnrc was used;[42] this code makes use of the XCOM database for cross-section data.[43] Dose calculations using the MC method involves two important steps.

(1) Creating an incident beam fluence map at some distance from the x-ray source.
(2) Transporting photons from the fluence map through a simulation sample (a biological tissuelike material).

Typically, an x-ray beam emitted from a conventional x-ray tube consists of the bremsstrahlung spectrum and characteristic peaks that correspond to the anode material of the x-ray tube [e.g., 22 keV (Ag)]. However, the broad bandwidths of energies produced by a conventional x-ray source are filtered in our instrument via a monochromator. The resulting x-ray beam that traverses the sample consists of monoenergetic parallel x rays. As a result, we have chosen to use 22 keV monoenergetic parallel beam in our calculations to represent the x-ray beam produced by our instrument.

The simulations were performed on a $10 \times 10 \times 6$ cm$^3$ tissuelike material for $5 \times 10^7$ iterations. The field size for the DEXI instrument is $1 \times 6$ cm$^2$ stripe. In order to image a sample that has a larger surface area than that of the x-ray beam field of view, the sample needs to be scanned through the monoenergetic beam. To simulate this type of procedure, several $1 \times 6$ cm$^2$ "stripes" aligned next to each other were used. Side scatter from one stripe to the next could potentially cause artifacts such as periodic fluctuations within the calculated field of view. However, the calculations show that a scattering equilibrium is established between neighboring stripes producing a homogenous field of x rays. These simulations were performed for a $6 \times 6$ cm$^2$ field size (corresponding to six neighboring stripes).

MC simulations were performed to produce a three-dimensional dose per incident fluence distribution matrix for the corresponding $10 \times 10 \times 6$ cm$^3$ tissuelike material. Combining this matrix with the experimentally measured incident surface fluence rate of $\Phi = 812$ mm$^{-2}$ s$^{-1}$ at 40 min exposure time per stripe results in a calculated total dose of 0.76 mGy for a $1 \times 6$ cm$^2$ single stripe (0.89 mGy for a six-stripe section measuring $6 \times 6$ cm$^2$).[44] A typical dose from conventional mammography is 3–4 mGy.[41] It is clear that we are delivering a significantly lower amount of radiation with our DEXI technology.

### D. Example data

The laboratory-based DEXI instrument described here was used to image a formalin preserved human cadaveric thumb. The sample was provided by the dissection laboratory of Rush University Medical Center, with Institutional Review Board approval. It is important to note that the aim of the work presented here is not to provide new anatomical findings of a human thumb, but rather to illustrate the capability of the instrument used to image the specimen.

The thumb which measures approximately $2 \times 3 \times 6$ cm$^3$ was imaged in air under ambient conditions. Images of the specimen were taken using 15 analyzer positions with an exposure time of 240 s per angular position. The thumb was translated horizontally three times due to it being wider than the $12 \times 60$ mm$^2$ x-ray beam field of view.

Figure 2 shows four DEX images of the thumb positioned upright and perpendicular with respect to the diffraction plane of our instrument. The calculated absorption image presented in Fig. 2(a) is representative of an absorption image taken by a conventional clinical x-ray source. The primary structures that are observed in the absorption image are both the proximal and distal phalanges (labeled I and II) and the boundary between the skin of the thumb and the ambient air. Tendons and other soft tissues are not observed in this type of contrast image.

Utilizing other contrast mechanisms, i.e., refraction, extinction and scattering, additional anatomical structures of the thumb are observed. Features such as the flexor pollicis longus tendon (III), connective tissue of the fat pad (IV), and blood vessels (V) are detected [Figs. 2(b)–2(d)]. The refraction image displays the most structural detail out of the four

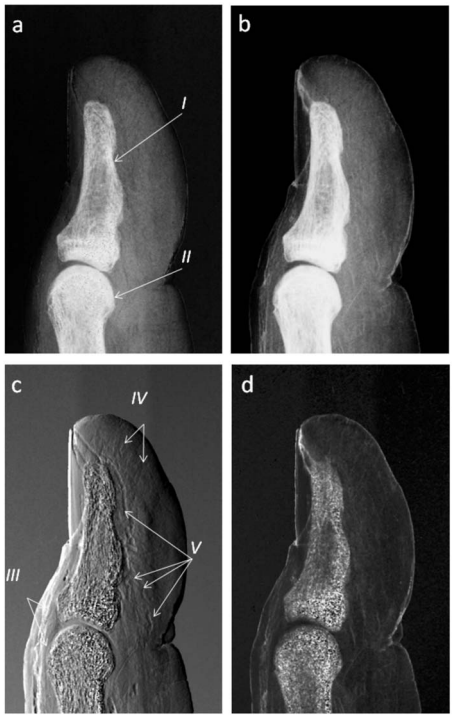


FIG. 2. A DEXI data set of a human cadaveric thumb (measuring $\sim 2 \times 3 \times 6$ $cm^3$): (a) calculated absorption image, (b) extinction image, (c) refraction image, and (d) scattering image. Observed anatomical structures: (I and II) proximal and distal phalanges; (III) flexor pollicis longus tendon; (IV) connective tissue; and (V) blood vessels.

DEX images.

It is important to note the inherent registry of both hard (i.e., bone) and soft tissue (i.e., tendons) using DEXI technology. This type of overlap provides a unique perspective for determining the relative positions of the internal structures of a sample. However, it is also important to mention that depending upon how a particular feature is positioned relative to the diffraction plane of the instrument it may not be optimally observed in the DEX images. Features that are oriented perpendicular (vertical) to the diffraction plane are best visible in the corresponding refraction image; however, structures that are parallel to the diffraction plane (horizontal) are not. As a result, automated positioning algorithms are currently being pursued in which the sample can be rotated about multiple axes providing a means of minimizing this imaging effect.

## IV. CONCLUSION

We have presented the design and application of a new laboratory-based (DEXI) system that has been used to image a human cadaveric thumb. A 2.2 kW silver anode x-ray tube was integrated with a compact, vibration-isolated, analyzer-based system. This table-top machine is capable of producing high-resolution DEX images without the use of a synchrotron radiation source. With an experimentally determined LSF of $160 \pm 7$ $\mu$m in the horizontal direction and $153 \pm 7$ $\mu$m in the vertical direction, our DEXI instrument has demonstrated the capability to detect both hard and soft tissues with simultaneous anatomical registry. The DEX images reveal anatomical structures that are normally undetectable using conventional x-ray techniques, while using far less radiation exposure to obtain the high contrast images. These preliminary results give great promise for the use of DEXI in a laboratory or clinical setting and provide a new state-of-the-art method for noninvasive imaging.

## ACKNOWLEDGMENTS

We would like to thank the Indiana 21st Century Research and Technology fund and the Indiana Economic Development Corporation for providing the financial support for this work.

[1] D. Chapman, W. Thomlinson, R. E. Johnston, D. Washburn, E. Pisano, N. Gmür, Z. Zhong, R. Menk, F. Arfelli, and D. Sayers, Phys. Med. Biol. **42**, 2015 (1997).
[2] O. Oltulu, Z. Zhong, M. Hasnah, M. N. Wernick, and D. Chapman, J. Phys. D **36**, 2152 (2003).
[3] D. Chapman, I. Nesch, M. Hasnah, and T. Morrison, Nucl. Instrum. Methods Phys. Res. A **562**, 461 (2006).
[4] C. Giles, M. G. Hönnicke, R. T. Lopes, H. S. Rocha, O. D. Gonçalves, I. Mazzaro, and C. Cusatis, J. Synchrotron Radiat. **10**, 421 (2003).
[5] M. G. Hönnicke and C. Cusatis, Rev. Sci. Instrum. **78**, 113708 (2007).
[6] M. N. Wernick, O. Wirjadi, D. Chapman, Z. Zhong, N. P. Galatsanos, Y. Yang, J. G. Brankov, O. Oltulu, M. A. Anastasio, and C. Muehleman, Phys. Med. Biol. **48**, 3875 (2003).
[7] G. Khelashvili, J. G. Brankov, D. Chapman, M. A. Anastasio, Y. Yang, Z. Zhong, and M. N. Wernick, Phys. Med. Biol. **51**, 221 (2006).
[8] C. Y. Chou, M. A. Anastasio, J. G. Brankov, M. N. Wernick, E. M. Brey, D. M. Connor, and Z. Zhong, Phys. Med. Biol. **52**, 1923 (2007).
[9] F. A. Dilmanian, Z. Zhong, B. Ren, X. Y. Wu, L. D. Chapman, I. Orion, and W. C. Thomlinson, Phys. Med. Biol. **45**, 933 (2000).
[10] J. G. Brankov, M. N. Wernick, Y. Yang, J. Li, C. Muehleman, Z. Zhong, and M. A. Anastasio, Med. Phys. **33**, 278 (2006).
[11] L. Rigon, A. Astolfo, F. Arfelli, and R. H. Menk, Eur. J. Radiol. **68**, S3 (2008).
[12] M. O. Hasnah, C. Parham, E. D. Pisano, Z. Zhong, O. Oltulu, and D. Chapman, Med. Phys. **32**, 549 (2005).
[13] M. N. Wernick, Y. Yang, I. Mondal, D. Chapman, M. Hasnah, C. Parham, E. Pisano, and Z. Zhong, Phys. Med. Biol. **51**, 1769 (2006).
[14] R. Lewis, Phys. Med. Biol. **42**, 1213 (1997).
[15] R. Meuli, Y. Hwu, J. H. Je, and G. Margaritondo, Eur. Radiol. **14**, 1550 (2004).
[16] J. Mollenhauer, M. E. Aurich, Z. Zhong, C. Muehleman, A. A. Cole, M. Hasnah, O. Oltulu, K. E. Kuettner, A. Margulis, and L. D. Chapman, Osteoarthritis Cartilage **10**, 163 (2002).
[17] J. Li, Z. Zhong, R. Lidtke, K. E. Kuettner, C. Peterfy, E. Aliyeva, and C. Muehleman, J. Anat. **202**, 463 (2003).
[18] R. A. Lewis, C. J. Hall, A. P. Hufton, S. Evans, R. H. Menk, F. Arfelli, L. Rigon, G. Tromba, D. R. Dance, I. O. Ellis, A. Evans, E. Jacobs, S. E. Pinder, and K. D. Rogers, Br. J. Radiol. **76**, 301 (2003).
[19] C. Muehleman, J. Li, M. Wernick, J. Brankov, K. Kuettner, and Z. Zhong, J. Musculoskeletal and Neuronal Interact. **4**, 369 (2004).
[20] C. Muehleman, D. R. Sumner, and Z. Zhong, J. Am. Podiatr. Med. Assoc. **94**, 453 (2004).
[21] J. Li, Z. Zhong, R. Lidtke, K. E. Kuettner, C. Peterfy, E. Aliyeva, and C. Muehleman, J. Am. Podiatr. Med. Assoc. **94**, 315 (2004).
[22] S. Majumdar, A. S. Issever, A. Burghardt, J. Lotz, F. Arfelli, L. Rigon, G. Heitner, and R. H. Menk, Eur. Radiol. **14**, 1440 (2004).
[23] J. Li, J. M. Williams, Z. Zhong, K. E. Kuettner, M. Aurich, J. Mollenhauer, and C. Muehleman, Osteoarthritis Cartilage **13**, 187 (2005).
[24] D. M. Connor, D. Sayers, D. R. Sumner, and Z. Zhong, Phys. Med. Biol. **51**, 3283 (2006).
[25] C. Muehleman, J. Li, and Z. Zhong, Osteoarthritis Cartilage **14**, 882 (2006).
[26] A. Wagner, A. Sachse, M. Keller, M. Aurich, W. D. Wetzel, P. Hortschansky, K. Schmuck, M. Lohmann, B. Reime, J. Metge, F. Arfelli, R. Menk, L. Rigon, C. Muehleman, A. Bravin, P. Coan, and J. Mollenhauer, Phys. Med. Biol. **51**, 1313 (2006).
[27] C. Muehleman, J. Li, Z. Zhong, J. G. Brankov, and M. N. Wernick, J. Anat. **208**, 115 (2006).
[28] C. Muehleman, J. Li, A. Schiff, and Z. Zhong, J. Am. Podiatr. Med. Assoc.

**99**, 95 (2009).
[29] C. Muehleman, L. D. Chapman, K. E. Kuettner, J. Rieff, J. A. Mollenhauer, K. Massuda, and Z. Zhong, Anat. Rec. Part A **272A**, 392 (2003).
[30] M. J. Kitchen, R. A. Lewis, N. Yagi, K. Uesugi, D. Paganin, S. B. Hooper, G. Adams, S. Jureczek, J. Singh, C. R. Christensen, A. P. Hufton, C. J. Hall, K. C. Cheung, and K. M. Pavlov, Br. J. Radiol. **78**, 1018 (2005).
[31] M. E. Kelly, R. C. Beavis, D. R. Fourney, E. Schültke, C. Parham, B. H. Juurlink, Z. Zhong, and L. D. Chapman, Can. Assoc. Radiol. J. **57**, 204 (2006).
[32] K. Noda-Saita, A. Yoneyama, Y. Shitaka, Y. Hirai, K. Terai, J. Wu, T. Takeda, K. Hyodo, N. Osakabe, T. Yamaguchi, and M. Okada, Neuroscience **138**, 1205 (2006).
[33] D. Chapman, E. Pisano, W. Thomlinson, Z. Zhong, R. E. Johnston, D. Washburn, D. Sayers, and K. Malinowska, Breast Dis. **10**, 197 (1998).
[34] E. D. Pisano, R. E. Johnston, D. Chapman, J. Geradts, M. V. Iacocca, C. A. Livasy, D. B. Washburn, D. E. Sayers, Z. Zhong, M. Z. Kiss, and W. C. Thomlinson, Radiology **214**, 895 (2000).
[35] M. Z. Kiss, D. E. Sayers, Z. Zhong, C. Parham, and E. D. Pisano, Phys. Med. Biol. **49**, 3427 (2004).
[36] S. Fiedler, A. Bravin, J. Keyriläinen, M. Fernández, P. Suortti, W. Thomlinson, M. Tenhunen, P. Virkkunen, and M. Karjalainen-Lindsberg, Phys. Med. Biol. **49**, 175 (2004).
[37] A. Bravin, J. Keyriläinen, M. Fernández, S. Fiedler, C. Nemoz, M. L. Karjalainen-Lindsberg, M. Tenhunen, P. Virkkunen, M. Leidenius, K. von Smitten, P. Sipilä, and P. Suortti, Phys. Med. Biol. **52**, 2197 (2007).
[38] H. S. Rocha, G. R. Pereira, P. Faria, G. Kellermann, I. Mazzaro, G. Tirao, C. Giles, and R. T. Lopes, Eur. J. Radiol. **68**, S37 (2008).
[39] L. W. Young, C. Parham, Z. Zhong, D. Chapman, and M. J. Reaney, J. Exp. Bot. **58**, 2513 (2007).
[40] I. N. Nesch and T. I. Morrison, U.S. Patent No. 7,107,693 B2 (19 September 2006).
[41] D. J. Brenner and E. J. Hall, N. Engl. J. Med. **357**, 2277 (2007).
[42] http://www.irs.inms.nrc.ca/EGSnrc/EGSnrc.html.
[43] http://www.physics.nist.gov/PhysRefData/Xcom/Text/XCOM.html.
[44] At 22 keV contributions from neighboring areas to the total dose were found to be negligible (on the order of 1%); as a result, background scattering effects from neighboring areas can be ignored when working at this energy.